Magnetic helicity fluxes in dynamos from rotating inhomogeneous turbulence

Axel Brandenburg[1, 2, 3, 4] and Ethan T. Vishniac[5]

[1]*Nordita, KTH Royal Institute of Technology and Stockholm University, Hannes Alfvéns väg 12, SE-10691 Stockholm, Sweden*
[2]*The Oskar Klein Centre, Department of Astronomy, Stockholm University, AlbaNova, SE-10691 Stockholm, Sweden*
[3]*McWilliams Center for Cosmology & Department of Physics, Carnegie Mellon University, Pittsburgh, PA 15213, USA*
[4]*School of Natural Sciences and Medicine, Ilia State University, 3-5 Cholokashvili Avenue, 0194 Tbilisi, Georgia*
[5]*Physics and Astronomy Department, Johns Hopkins University, Baltimore, MD 21218, USA*

ABSTRACT

We analyze direct numerical simulations of large-scale dynamos in inhomogeneous nonhelically-driven rotating turbulence with and without shear. The forcing is modulated so that the turbulent intensity peaks in the middle of the computational box and drops to nearly zero at the two ends above and below the midplane. A large-scale dynamo is driven by an α effect of opposite signs between the two hemispheres. In the presence of shear, the hemispheric magnetic helicity flux from small-scale fields becomes important and can even overcompensate for the magnetic helicity transferred by the α effect between large and small scales. This effect has not previously been observed in non-shearing simulations. Our numerical simulations show that the hemispheric magnetic helicity fluxes are nearly independent of the magnetic Reynolds number, but those between large and small scales, and the consequent dynamo effect, are still found to decrease with increasing Reynolds number—just like in nonshearing dynamos. However, in contrast to nonshearing dynamos, where the generated mean magnetic field declines with increasing magnetic Reynolds number, it is now found to remain independent of it. This suggests that catastrophic dynamo quenching is alleviated by the shear-induced hemispheric small-scale magnetic helicity fluxes that can even overcompensate the fluxes between large and small scales and thereby cause resistive contributions.

1. INTRODUCTION

Many astrophysical bodies harbour large-scale magnetic fields. Late-type stars and galaxies are the main examples where a dynamo converts kinetic energy into large-scale magnetic energy (Charbonneau 2014; Brandenburg & Ntormousi 2023). Disks around young stars and compact objects are additional examples, where the existence of large-scale magnetic fields has so far only been inferred from simulations (Armitage 2011; Jiang et al. 2014; Davis & Tchekhovskoy 2020). In all these cases, there is turbulence, the bodies rotate, and they are stratified in the sense that the density and/or the turbulent velocity vary in space. This, together with the overall rotation, causes the turbulence to become helical, which leads to an α effect (Parker 1955; Steenbeck et al. 1966), where the coefficient α relates

the mean electromotive force to the mean magnetic field. Also the magnetic field attains helicity, which affects the α effect (Pouquet et al. 1976). The underling theory has been the subject of textbooks (Moffatt 1978; Parker 1979; Krause & Rädler 1980; Zeldovich et al. 1983), but later it became clear that magnetic helicity conservation causes such dynamos to saturate at progressively lower values as the microphysical resistivity decreases or the conductivity increases (Gruzinov & Diamond 1996; Ji 1999; Kleeorin et al. 2000; Brandenburg 2001; Vishniac & Cho 2001; Field & Blackman 2002; Blackman & Brandenburg 2002). The resulting mean magnetic field would then be very weak for astrophysically relevant resistivities.

Blackman & Field (2000) coined the term catastrophic quenching, which, in its original form, refers to the actual value of α becoming very small at low resistivities. In particular, numerical simulations by Cattaneo & Hughes (1996) have shown that for mean

fields defined as volume averages, the value of α diminishes to zero as the conductivity increases. It was therefore thought to be difficult to explain the generation of the large-scale magnetic fields observed in many astrophysical bodies with an α effect. It quickly became clear that the problem of catastrophic quenching is connected with the homogeneity of the turbulence in such simple numerical setups. In those cases, there can be no magnetic helicity flux and magnetic helicity is then well conserved in the limit of large conductivity. To avoid this difficulty, Vishniac & Cho (2001) envisaged an α effect that is computed from a specifically designed magnetic helicity flux such that the magnetic helicity is conserved exactly. However, the anticipated magnetic helicity fluxes have not yet been found in numerical simulations (Hubbard & Brandenburg 2012). With just inhomogeneous turbulence, many numerical simulations show that the amplitude of the resulting mean magnetic field decreases with increasing conductivity (Del Sordo et al. 2013; Rincon 2021; Bermudez & Alexakis 2022). This phenomenon is then generally also still referred to as the catastrophic quenching problem, even though α itself may no longer be catastrophically small. On the other hand, corresponding analytic calculations of the mean magnetic helicity fluxes by Kleeorin & Rogachevskii (2022) have not shown a dependence of the magnetic helicity flux on the microphysical conductivity. The reason for catastrophic quenching remains therefore obscured.

Many previous numerical simulations employed helical forcing. The purpose of the present work is to avoid this by adopting a more natural setup in which a non-helical flow is being driven. Kinetic helicity of the flow can then emerge self-consistently as a result of stratification and rotation. We also consider the effect of shear and how it contributes to the α effect (Rüdiger & Brandenburg 2014). Shear may also be responsible for driving magnetic helicity fluxes (Vishniac & Cho 2001). In this paper, we focus on the analysis of the magnetic helicity fluxes resulting from a simulation in slab geometry with horizontal xy averages depending on time and disk height z. In the middle of the domain at $z = 0$, the averaged turbulent intensity has a maximum. The angular velocity vector points in the positive z direction, which allows us to associate the regions above and below the midplane with north and south. This geometry can also be applied to the two sides around the equator of a sphere, where the z coordinate corresponds to latitude.

For our numerical simulations, we employ the PENCIL CODE (Pencil Code Collaboration et al. 2021). Since it advances the magnetic vector potential, the magnetic field is always solenoid and the code is well suited for the task of analyzing magnetic helicity and its flux. Other codes that evolve instead the magnetic field and use divergence cleaning to keep the magnetic field solenoidal can spontaneously produce or destroy small-scale magnetic helicity (Brandenburg & Scannapieco 2020), although schemes have been devised to conserve magnetic helicity at the expense of modifying the magnetic field in neighboring places (Zenati & Vishniac 2023). The PENCIL CODE has also been used successfully in various earlier studies of magnetic helicity fluxes (Hubbard & Brandenburg 2010, 2011; Del Sordo et al. 2013; Brandenburg 2018a).

In Section 2, we describe our numerical simulations and the test-field method that is used to compute turbulent transfer coefficient. We also discuss the decomposition of magnetic helicity fluxes into contributions between hemispheres and between large and small scales. In Section 3, we describe the results without and with shear. We conclude in Section 4.

2. DESCRIPTION OF THE MODEL

2.1. *Governing equations*

We consider nonhelically driven inhomogeneous turbulence of an isothermal gas with constant sound speed c_s in the presence of rotation with the angular velocity vector $\boldsymbol{\Omega} \equiv (0, 0, \Omega)$. In some cases, we include an additional shear flow, $\boldsymbol{V} = (0, Sx, 0)$, where $S = -q\Omega$ is a constant and q is the shear parameter. Shear flows with $q < 2$ are Rayleigh-stable, but unstable to the MRI for $q > 0$; see Balbus & Hawley (1998) for a review. Keplerian shear corresponds to $q = 3/2$, while shear in galactic disks corresponds to $q = 1$ (Beck et al. 1996). The turbulence is stochastically driven with a forcing function $\boldsymbol{f}(\boldsymbol{x}, t)$, whose intensity is modulated in the z direction with a profile function $f_{\text{prof}}(z) = \cos^2(k_1 z/2)$, where $k_1 = 2\pi/L$ is the lowest wavenumber in a cube of size L^3. The forcing is applied on the right-hand side of the evolution equation for the velocity $\boldsymbol{U}$, which then reads (Brandenburg et al. 1995, 2008a)

$$\frac{\mathcal{D}\boldsymbol{U}}{\mathcal{D}t} = \boldsymbol{f}(\boldsymbol{x}, t) - \boldsymbol{U} \cdot \boldsymbol{\nabla}\boldsymbol{U} - SU_x\hat{\boldsymbol{y}} - 2\boldsymbol{\Omega} \times \boldsymbol{U}$$
$$- c_s^2 \boldsymbol{\nabla} \ln \rho + \frac{1}{\rho}\left[\boldsymbol{J} \times \boldsymbol{B} + \boldsymbol{\nabla} \cdot (2\rho\nu\mathsf{S})\right], \quad (1)$$

where $\mathcal{D}/\mathcal{D}t = \partial/\partial t + \boldsymbol{V} \cdot \boldsymbol{\nabla}$ is the advective derivative with respect to the shear flow, ρ is the density, $\boldsymbol{B}$ is the magnetic field, $\boldsymbol{J} = \boldsymbol{\nabla} \times \boldsymbol{B}/\mu_0$ is the current density, μ_0 is the vacuum permeability, ν is the viscosity, and S is the traceless rate-of-strain tensor with the components $\mathsf{S}_{ij} = (\partial_i U_j + \partial_j U_i)/2 - \delta_{ij}\boldsymbol{\nabla} \cdot \boldsymbol{U}/3$. The tensor S is not to be confused with the constant scalar S, which denotes the uniform background shear when $q \neq 0$. The logarithmic density obeys the continuity equation in the

form

$$\frac{\mathcal{D}\ln\rho}{\mathcal{D}t} = -\boldsymbol{U}\cdot\boldsymbol{\nabla}\ln\rho - \boldsymbol{\nabla}\cdot\boldsymbol{U}. \qquad (2)$$

The magnetic field $\boldsymbol{B} = \boldsymbol{\nabla}\times\boldsymbol{A}$ is solved in terms of the magnetic vector potential $\boldsymbol{A}$,

$$\frac{\mathcal{D}\boldsymbol{A}}{\mathcal{D}t} = -SA_y\hat{\boldsymbol{x}} - \boldsymbol{E} - \boldsymbol{\nabla}\Phi, \qquad (3)$$

where $\boldsymbol{E} = \eta\mu_0\boldsymbol{J} - \boldsymbol{U}\times\boldsymbol{B}$ is the electric field with $SA_y\hat{\boldsymbol{x}} \equiv \boldsymbol{E}_\mathrm{S}$ being the contribution from the shear, η is the magnetic diffusivity, and Φ is the electrostatic potential. In Equation (3), we have adopted the advecto-resistive gauge, in which $\Phi = -V_yA_y - \eta\boldsymbol{\nabla}\cdot\boldsymbol{A}$ (Candelaresi et al. 2011). As shown in Brandenburg et al. (1995), the inclusion of the advective term V_yA_y is necessary for being able to adopt shearing–periodic boundary conditions. This means that the magnetic diffusion operator reduces to $\eta\nabla^2\boldsymbol{A}$; see Candelaresi et al. (2011) for further details. In some cases, we also compute the vector potential in the Coulomb gauge, $\boldsymbol{A}^\mathrm{Cou} = \boldsymbol{A} - \boldsymbol{\nabla}\Lambda$, by solving $\nabla^2\Lambda = \boldsymbol{\nabla}\cdot\boldsymbol{A}$ with appropriate boundary conditions.

The nonhelical forcing function $f(\boldsymbol{x},t)$ is given by (Haugen et al. 2004)

$$f(\boldsymbol{x},t) = f_0c_\mathrm{s}\left(c_\mathrm{s}k/\delta t\right)^{1/2}\frac{\boldsymbol{e}\times\boldsymbol{k}}{|\boldsymbol{e}\times\boldsymbol{k}|}\,e^{\mathrm{i}\boldsymbol{k}(t)\cdot\boldsymbol{x}+\mathrm{i}\varphi(t)}, \qquad (4)$$

where $\boldsymbol{e}$ is a random vector that is not aligned with $\boldsymbol{k}$, $\varphi(t)$ is a random phase ($|\varphi| \leq \pi$), and f_0 is the amplitude. At each time step, a new forcing vector $\boldsymbol{k}(t)$ is chosen randomly from a set of wavevectors $\boldsymbol{k}$ whose lengths $|\boldsymbol{k}|$ lie in a narrow band $k_\mathrm{f} - \delta k/2 \leq k < k_\mathrm{f} + \delta k/2$, where $k_\mathrm{f} = 8$ and $\delta k = 1$ is used for all the runs discussed in this paper.

To analyze the possibility of large-scale dynamo action, it is useful to compute planar averages. Owing to the inhomogeneity in the z direction, we adopt xy averages, which are denoted by an overbar, e.g., $\overline{U}(z,t) = \int\boldsymbol{u}(\boldsymbol{x},t)\,\mathrm{d}x\,\mathrm{d}y/L^2$. Fluctuations about the average are then denoted by lowercase symbols, e.g., $\boldsymbol{u} = \boldsymbol{U} - \overline{\boldsymbol{U}}$, $\boldsymbol{b} = \boldsymbol{B} - \overline{\boldsymbol{B}}$, and $\boldsymbol{j} = \boldsymbol{J} - \overline{\boldsymbol{J}}$.

2.2. Control parameters and initial conditions

The value of the overall root-mean square (rms) velocity u_rms is characterized by the Mach number, $\mathrm{Ma} = u_\mathrm{rms}/c_\mathrm{s}$. When there is shear, the value of u_rms does not include this shear flow. Since we are here not interested in studying compressibility effects, we adopt subsonic Mach numbers and take $\mathrm{Ma} \lesssim 0.1$ for all runs. The values of ν and η are characterized by the fluid and magnetic Reynolds numbers,

$$\mathrm{Re} = u_\mathrm{rms}/\nu k_\mathrm{f} \quad\text{and}\quad \mathrm{Re_M} = u_\mathrm{rms}/\eta k_\mathrm{f}, \qquad (5)$$

respectively. The ratio $\mathrm{Pr_M} = \nu/\eta$ is the magnetic Prandtl number. In the following, we vary $\mathrm{Pr_M}$ by keeping the value of Re fixed. Another control parameter is the relative forcing wavenumber, k_f/k_1. The amount of rotation and shear are quantified by the Coriolis and shear numbers,

$$\mathrm{Co} = 2\Omega/u_\mathrm{rms}k_\mathrm{f} \quad\text{and}\quad \mathrm{Sh} = S/u_\mathrm{rms}k_\mathrm{f}, \qquad (6)$$

respectively. As initial condition, we use $\boldsymbol{U} = \ln\rho/\rho_0 = 0$, so the initial density is equal to some reference density ρ_0.

The initial magnetic vector potential is calculated from a weak Gaussian-distributed field with an rms value B_rms such that the rms Alfvén speed $v_\mathrm{A} = B_\mathrm{rms}/\sqrt{\mu_0\rho_0}$ is a small fraction of c_s. When $\mathrm{Re_M}$ exceeds a certain critical value, there is dynamo action, i.e., $v_\mathrm{A}/c_\mathrm{s}$ grows exponentially and saturates eventually at a value around 0.1. Instead of quantifying $v_\mathrm{A}/c_\mathrm{s}$, it is useful to quantify the ratio $v_\mathrm{A}/u_\mathrm{rms}$, or, equivalently, the value of B_rms in units of the equipartition field strength, $B_\mathrm{eq} = \sqrt{\mu_0\rho_0}\,u_\mathrm{rms}$. The rms value of the large-scale field is denoted by $\overline{B}_\mathrm{rms}$.

Owing to the presence of rotation and stratification of the turbulent intensity, we expect the generation of kinetic helicity, $\overline{\boldsymbol{\omega}\cdot\boldsymbol{u}}$, where $\boldsymbol{\omega} = \boldsymbol{\nabla}\times\boldsymbol{u}$ is the vorticity of the fluctuating velocity. Following Jabbari et al. (2014), we determine the resulting kinetic helicity in terms of the non-dimensional ratio

$$\epsilon_\mathrm{f}(z) = \overline{\boldsymbol{\omega}\cdot\boldsymbol{u}}/u_\mathrm{rms}^2 k_\mathrm{f}, \qquad (7)$$

which is characterized primarily by the amplitude of its variation, defined here as

$$\epsilon_\mathrm{f0} = 2\left\langle\epsilon_\mathrm{f}(z)\sin k_1z\right\rangle. \qquad (8)$$

As in Jabbari et al. (2014), we expect ϵ_f0 to increase linearly with increasing rotation rate and with increasing stratification of turbulent intensity, provided these values are not too large.

The simulations are performed with the PENCIL CODE (Pencil Code Collaboration et al. 2021). Numerical results are usually presented as averages over a statistically steady stretch in time. Error margins are estimated as the largest departure over any one third of the full time series.

2.3. Quasi-kinematic test-field method

To characterize the nature of large-scale dynamo action, we need to obtain the mean-field dynamo coefficients that characterize the dependence of the mean electromotive force $\overline{\boldsymbol{\mathcal{E}}}$ on $\overline{\boldsymbol{B}}$ and $\overline{\boldsymbol{J}}$. The most accurate choice is the test-field method (Schrinner et al. 2005, 2007; Brandenburg 2005; Brandenburg et al. 2008c).

In the test-field method, we solve the equations for the fluctuations $\boldsymbol{b}_\mathrm{T}$ that result from a certain test field $\overline{\boldsymbol{B}}_\mathrm{T}$. We represent it by $\boldsymbol{b}_\mathrm{T} = \boldsymbol{\nabla} \times \boldsymbol{a}_\mathrm{T}$ and solve for the vector potential $\boldsymbol{a}_\mathrm{T}$, which, in the Weyl (or temporal) gauge with zero electrostatic potential, obeys

$$\frac{\partial \boldsymbol{a}_\mathrm{T}}{\partial t} = \boldsymbol{u} \times \overline{\boldsymbol{B}}_\mathrm{T} + \overline{\boldsymbol{U}} \times \boldsymbol{b}_\mathrm{T} + \boldsymbol{u} \times \boldsymbol{b}_\mathrm{T} - \overline{\boldsymbol{u} \times \boldsymbol{b}_\mathrm{T}} + \eta \nabla^2 \boldsymbol{a}_\mathrm{T}. \quad (9)$$

This allows us to compute $\overline{\boldsymbol{\mathcal{E}}}^\mathrm{T} = \overline{\boldsymbol{u} \times \boldsymbol{b}_\mathrm{T}}$. We adopt the parameterization $\overline{\mathcal{E}}_i^\mathrm{T} = \alpha_{ij} \overline{B}_j^\mathrm{T} - \eta_{ij} \mu_0 \overline{J}_j^\mathrm{T}$. Since only the x and y components are significant, we have 8 unknowns for the 4 components of α_{ij} and the 4 components of η_{ij}. To obtain all unknowns, we use the 4 vectorial test fields $\overline{\boldsymbol{B}}_\mathrm{T} = (c, 0, 0)$, $(s, 0, 0)$, $(0, c, 0)$, and $(0, s, 0)$, where $c = \cos k_\mathrm{T} z$ and $s = \sin k_\mathrm{T} z$. Since only the x and y components are significant, we have exactly 8 independent equations for the 8 unknowns. We choose $k_\mathrm{T} = k_1$ and refer to Brandenburg et al. (2008c) regarding the significance of also studying $k_\mathrm{T} > k_1$ to obtain full integral kernels in a parameterization involving integral kernels.

When $\boldsymbol{u}$ in Equation (9) is a solution of the nonlinear Equation (1) with the Lorentz force included, we talk about the quasi-kinematic test-field method. This method is nonlinear in the sense that it describes correctly the modifications of the velocity field in response to the actual magnetic field in the simulations (Brandenburg et al. 2008b; Karak et al. 2014). However, it is not fully nonlinear in the sense that it does not include the fluctuating magnetic field from a small-scale dynamo (Rheinhardt & Brandenburg 2010; Käpylä et al. 2022). On the other hand, there are so far no clear cases of practical interest where the quasi-kinematic method is known to fail; see Brandenburg (2018b) for a review. The only exception is the case where magnetic fluctuations are produced by applying externally maintained currents to drive the system. Those cases are mainly of academic interest and not relevant to our problem at hand. The success of the quasi-kinematic method lies probably in the fact that the small-scale dynamo-generated magnetic fields are not well correlated with the large-scale field.

In the present case, the time-averaged turbulent transport coefficients depend on z. In addition to plotting the individual components of α_{ij} and η_{ij}, we also compute the traces $\alpha \equiv (\alpha_{xx} + \alpha_{yy})/2$ and $\eta_\mathrm{t} \equiv (\eta_{xx} + \eta_{yy})/2$, as well as the antisymmetric parts, $\gamma \equiv (\alpha_{yx} - \alpha_{xy})/2$ and $\delta \equiv (\eta_{xy} - \eta_{yx})/2$. In the following, we fit η_t to Legendre polynomials of $\cos k_1 z$. Since these are orthogonal polynomials, a decline of the coefficients with increasing order can be interpreted as convergence. Another quantity of interest is the z-dependent dynamo number,

$C_\alpha = \alpha / \eta_\mathrm{t} k_1$. In the present case, it turns out that, to a good approximation, it has a linear profile. The values and slopes are given in tabular form below.

2.4. *Mean-field evolution*

To assess the importance of the aforementioned turbulent transport coefficients α, η_t, γ, and δ, we consider numerical mean-field models, where we can rescale the coefficients to learn about their relative importance. In that case, we solve the 1–D mean-field equation, again in the Weyl gauge,

$$\frac{\partial \overline{\boldsymbol{A}}}{\partial t} = \alpha \overline{\boldsymbol{B}} - \eta_\mathrm{T} \mu_0 \overline{\boldsymbol{J}} + \boldsymbol{\gamma} \times \overline{\boldsymbol{B}} + \boldsymbol{\delta} \times \mu_0 \overline{\boldsymbol{J}} - S \overline{A}_y \hat{\boldsymbol{x}}, \quad (10)$$

where $\boldsymbol{\gamma} = (0, 0, \gamma)$ and $\boldsymbol{\delta} = (0, 0, \delta)$ are vectors that only have a z component and $\eta_\mathrm{T} = \eta_\mathrm{t} + \eta$ is the total magnetic diffusivity. It should be remembered, however, that the values and profiles of the turbulent transport coefficients have been computed under the assumption of steady mean fields. This is obviously not the case; see Hubbard & Brandenburg (2009) for the treatment of time-dependent mean fields.

2.5. *Magnetic helicity fluxes*

The saturation level of the resulting mean magnetic field is known to be severely limited by the ability to shed magnetic helicity from the dynamo through magnetic helicity fluxes; see Zhou & Blackman (2024) for a recent assessment. It is therefore of interest to consider the evolution equation for the magnetic helicity balance separately for the large-scale and small-scale contributions by splitting the total mean magnetic density, $\overline{\boldsymbol{A} \cdot \boldsymbol{B}}$, into two parts: $\overline{\boldsymbol{A}} \cdot \overline{\boldsymbol{B}}$ and $\overline{\boldsymbol{a} \cdot \boldsymbol{b}}$. The evolution equation for $\overline{\boldsymbol{A} \cdot \boldsymbol{B}}$ is obtained by dotting Equation (3) with $\boldsymbol{B}$ and adding its curl dotted with $\boldsymbol{A}$, which yields

$$\frac{\partial}{\partial t} \overline{\boldsymbol{A} \cdot \boldsymbol{B}} = -2 \overline{\boldsymbol{E} \cdot \boldsymbol{B}} - \boldsymbol{\nabla} \cdot \overline{\boldsymbol{\mathcal{F}}}, \quad (11)$$

where $\overline{\boldsymbol{\mathcal{F}}} = \overline{\boldsymbol{E} \times \boldsymbol{A}} + \overline{\Phi \boldsymbol{B}}$ is the total magnetic helicity flux. Note also that $\overline{\boldsymbol{E} \cdot \boldsymbol{B}} = \eta \nu_0 \overline{\boldsymbol{J} \cdot \boldsymbol{B}}$, i.e., the induction term does not contribute. The evolution equation for $\overline{\boldsymbol{A}} \cdot \overline{\boldsymbol{B}}$ is obtained from the evolution equation for the mean field, $\partial \overline{\boldsymbol{A}} / \partial t = -\overline{\boldsymbol{E}} - \boldsymbol{\nabla} \overline{\Phi}$, where

$$\overline{\boldsymbol{E}} = \eta \mu_0 \overline{\boldsymbol{J}} - \overline{\boldsymbol{U}} \times \overline{\boldsymbol{B}} - \overline{\boldsymbol{\mathcal{E}}} \quad (12)$$

is the averaged electric field and $\overline{\boldsymbol{\mathcal{E}}} = \overline{\boldsymbol{u} \times \boldsymbol{b}}$ is the mean electromotive force from the fluctuating fields. This yields

$$\frac{\partial}{\partial t} \overline{\boldsymbol{A}} \cdot \overline{\boldsymbol{B}} = 2 \overline{\boldsymbol{\mathcal{E}}} \cdot \overline{\boldsymbol{B}} - 2 \eta \mu_0 \overline{\boldsymbol{J}} \cdot \overline{\boldsymbol{B}} - \boldsymbol{\nabla} \cdot \overline{\boldsymbol{\mathcal{F}}}_\mathrm{m}, \quad (13)$$

where $\overline{\boldsymbol{\mathcal{F}}}_\mathrm{m} = \overline{\boldsymbol{E}} \times \overline{\boldsymbol{A}} + \overline{\Phi} \overline{\boldsymbol{B}}$ is the magnetic helicity flux from the mean field. Note, however, that in our cases

$\overline{B}_z = 0$ at all times owing to the fact that $\boldsymbol{\nabla} \cdot \overline{\boldsymbol{B}} = 0$, the use of planar averages, and the fact that $\overline{B}_z = 0$ initially. Therefore, $\overline{\Phi}\,\overline{\boldsymbol{B}} = 0$. Furthermore, the mean-field shear contribution, $\overline{\boldsymbol{E}}_{\rm S}$, to the mean electric field only leads to a lateral magnetic helicity flux and is therefore irrelevant.

Finally, the evolution equation for $\overline{\boldsymbol{a} \cdot \boldsymbol{b}}$ is obtained from the difference $\overline{\boldsymbol{A} \cdot \boldsymbol{B}} - \overline{\boldsymbol{A}} \cdot \overline{\boldsymbol{B}}$, which yields

$$\frac{\partial}{\partial t}\overline{\boldsymbol{a} \cdot \boldsymbol{b}} = -2\overline{\boldsymbol{\mathcal{E}}} \cdot \overline{\boldsymbol{B}} - 2\eta\mu_0\overline{\boldsymbol{j} \cdot \boldsymbol{b}} - \boldsymbol{\nabla} \cdot \overline{\boldsymbol{\mathcal{F}}}_{\rm f}, \qquad (14)$$

where $\overline{\boldsymbol{\mathcal{F}}}_{\rm f} = \overline{\boldsymbol{e} \times \boldsymbol{a}} + \overline{\phi\boldsymbol{b}}$ is the magnetic helicity flux of the fluctuating field, $\boldsymbol{e} = \boldsymbol{E} - \overline{\boldsymbol{E}}$ is the fluctuating electric field, and $\phi = V_y a_y - \eta\boldsymbol{\nabla} \cdot \boldsymbol{a}$. Contrary to Brandenburg (2018a), we use here the more natural and more compact notation where $\overline{\boldsymbol{\mathcal{E}}}$ is included in the definition of $\boldsymbol{E}$; see Equation (12).

In the statistically steady state, we can drop the time derivative. Instead of considering volume-integrated quantities separately for the northern and southern hemispheres, it is convenient to plot them as fluxes in terms of undetermined integrals,

$$\int_{z_-}^{z} 2\eta\mu_0\overline{\boldsymbol{J}} \cdot \overline{\boldsymbol{B}}\,{\rm d}z = +\int_{z_-}^{z} 2\overline{\boldsymbol{\mathcal{E}}} \cdot \overline{\boldsymbol{B}}\,{\rm d}z - \overline{\mathcal{F}}_{{\rm m}z}, \qquad (15)$$

$$\int_{z_-}^{z} 2\eta\mu_0\overline{\boldsymbol{j} \cdot \boldsymbol{b}}\,{\rm d}z = -\int_{z_-}^{z} 2\overline{\boldsymbol{\mathcal{E}}} \cdot \overline{\boldsymbol{B}}\,{\rm d}z - \overline{\mathcal{F}}_{{\rm f}z}, \qquad (16)$$

in the range $z_- \leq z \leq z_+$, where $z_\pm = \pm\pi/k_1$ are the upper and lower boundaries of the cube. In the following, we refer to these as "integrated terms".

Note that in both Equations (15) and (16) there are three terms of which two are manifestly gauge-invariant. Therefore, also the third term, $\overline{\mathcal{F}}_{{\rm m}z}$ and $\overline{\mathcal{F}}_{{\rm m}z}$ in each equation, respectively, must be gauge-invariant. This argument was already applied by Hubbard & Brandenburg (2010) in their work on magnetic helicity fluxes from a dynamo embedded in a conducting halo.

It is convenient to present the magnetic helicity fluxes in normalized form. For the following, we define the reference flux as

$$F_{{\rm m}0} = \eta_{{\rm t}0}k_1\int_{z_-}^{z_+}\overline{\boldsymbol{B}}^2\,{\rm d}z. \qquad (17)$$

This is analogous to the work of Brandenburg (2018a), except that there k_1^2 instead of k_1 was written by mistake.

To compare the current helicity with the kinetic helicity, we define $\epsilon_{\rm f}^{\rm M}(z) = \overline{\boldsymbol{j} \cdot \boldsymbol{b}}/u_{\rm rms}^2 k_{\rm f}$ and its amplitude as $\epsilon_{{\rm f}0}^{\rm M} = 2\left\langle\epsilon_{\rm f}^{\rm M}(z)\sin k_1 z\right\rangle$. Finally, the ratio between the small-scale current and magnetic helicity densities
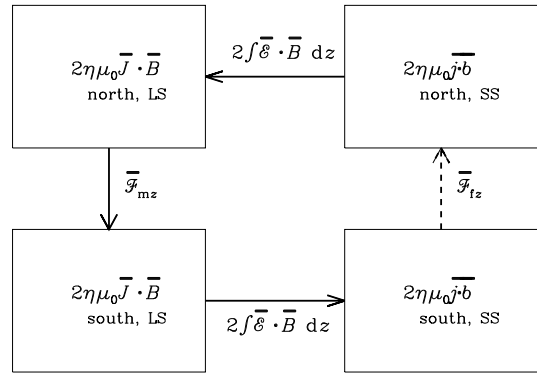
Figure 1. Sketch of the magnetic helicity fluxes between north and south (upper and lower boxes), and between large scales (LS, left) and small scales (SS, right). In the steady state, the four magnetic helicity reservoirs can still have sinks or sources because of the microphysical resistivity. This can still be important, especially at small scales, and therefore the small-scale magnetic helicity fluxes, $\overline{\boldsymbol{\mathcal{F}}}_{{\rm f}z}$, may not balance the $2\overline{\boldsymbol{\mathcal{E}}} \cdot \overline{\boldsymbol{B}}$ term, which is therefore indicated by the dashed arrow.

is characterized by the ratio $k_{\rm eff}^2 = \overline{\boldsymbol{j} \cdot \boldsymbol{b}}/\overline{\boldsymbol{a} \cdot \boldsymbol{b}}$, where the two terms have been computed from a sinusoidal fit, analogously to $\epsilon_{{\rm f}0}^{\rm M}$. These quantities are discussed in Section 3. It should be noted, however, that the departure of $k_{\rm eff}$ from the value of $k_{\rm f}$ is mainly a measure of the departure of the magnetic vector potential from the Coulomb gauge, because the term $\boldsymbol{\nabla} \cdot \boldsymbol{A}$ in the expression for $\boldsymbol{J} = -\nabla^2\boldsymbol{A} + \boldsymbol{\nabla}\boldsymbol{\nabla} \cdot \boldsymbol{A}$ can be important. By contrast, the ratio $\overline{(-\nabla^2\boldsymbol{a}) \cdot \boldsymbol{b}}/\overline{\boldsymbol{a} \cdot \boldsymbol{b}}$ is typically found to be close to the actual value of $k_{\rm f} = 8\,k_1$, even when the Coulomb gauge is not used.

2.6. Magnetic helicity cycle

In this section, we explain that there is a continuous flux of magnetic helicity both between hemispheres and between scales. This is illustrated in Figure 1.

Owing to the presence of rotation and a finite gradient in the turbulent intensity, an α effect is expected based on the formula by Steenbeck et al. (1966),

$$\alpha \approx -\ell^2\boldsymbol{\Omega} \cdot \boldsymbol{\nabla}\ln(\rho u_{\rm rms}), \qquad (18)$$

where ℓ is a suitable length scale. We refer here to Rüdiger & Kichatinov (1993) for analytical calculations based on the consideration of homogeneous background turbulence that is being affected by stratification and rotation, and Brandenburg et al. (2013) for simulation results over a broad range of astrophysical settings. Equation (18) predicts a positive (negative) value of α in the upper (lower) disk plane. This, in turn, implies negative (positive) kinetic helicities of the small-scale

Table 1. Summary of the results for our test-field runs. Run E has uniform shear with $q = 0.5$.

						$\overline{\eta_{t0}^{-1} \times}$									$- B_{eq}^{-1} \times -$	
Run	Sh	Re	Re$_M$	Pr$_M$	$\eta k_1/c_s$	$\eta_t^{(0)}$	$\eta_t^{(1)}$	$\eta_t^{(2)}$	$\eta_t^{(3)}$	$C_\alpha(z)$	$-\epsilon_{f0}$	ϵ_{f0}^M	k_{eff}	Co	B_{rms}	$\overline{B}_{rms}$
A	0	17.5	3.5	0.2	2.5×10^{-3}	0.80	0.89	0.17	0.01	$2.81\,z$	0.48	-0.06	8.8	1.78	0.52	0.43
B	0	16.9	16.9	1	5×10^{-4}	0.71	0.87	0.24	0.06	$2.52\,z$	0.47	-0.12	11	1.84	0.57	0.34
C	0	16.4	82	5	10^{-4}	0.71	0.87	0.24	0.06	$2.30\,z$	0.48	-0.14	14	1.91	0.58	0.22
D	0	15.8	158	10	5×10^{-5}	0.64	0.76	0.18	0.04	$2.22\,z$	0.47	-0.14	17	1.98	0.59	0.19
E	0.63	12.3	123	10	5×10^{-5}	0.49	0.45	0.01	0.04	$1.37\,z$	0.22	0.007	3.0	2.50	1.39	0.34

velocity and magnetic fields in the upper (lower) disk plane. It is known that, at least in the absence of shear, the magnetic helicity of the small-scale field is then also negative (positive) in the upper (lower) disk plane (Del Sordo et al. 2013; Rincon 2021). Assuming that small-scale magnetic helicity is transported down the gradient of the magnetic helicity density and/or magnetic energy density (Kleeorin & Rogachevskii 2022), we expect a small-scale magnetic helicity flux from south to north; see the dashed line in Figure 1. It is shown here as a dashed line, because in our simulations without shear, this flux appears to be too weak, while in our runs with shear, it appears to be too large to balance the corresponding fluxes at large scales.

There is also a magnetic helicity flux from small to large scales, which is given by the integral of $2\overline{\boldsymbol{\mathcal{E}}} \cdot \overline{\boldsymbol{B}}$. This term has a contribution $\alpha \overline{\boldsymbol{B}}^2$, which is positive in the north, but since it enters with a minus sign, the associated flux points from small to large scales, and in the opposite direction in the south where α is negative; see Figure 1.

3. RESULTS

We have performed a series of runs with different parameters; see Table 1 for a summary. In all cases without shear, we use 256^3 meshpoints and keep the viscosity fixed ($\nu k_1/c_s = 5 \times 10^{-4}$), so the level of turbulence stays unchanged, but Re$_M$ is increased by decreasing the value of η. This makes the dynamo stronger, so B_{rms}/B_{eq} increases. This quenches the velocity field, and therefore the values of Re decrease with increasing values of Pr$_M$. We notice, however, that, as Pr$_M$ and B_{rms}/B_{eq} increase, the normalized rms value of the mean field, $\overline{B}_{rms}/B_{eq}$, decreases. As already emphasized above, this is at the core of the problem of catastrophic quenching.

For Runs A–E, we also have obtained test-field results, while for Runs F–H, we have focussed on the analysis of the contributions to the magnetic helicity balance.

In some of those runs, we also increased the resolution. Those runs have uniform shear with $q = 0.5$. This choice is motivated by demanding that $|\boldsymbol{V}|/c_s$ does not exceed unity. The values of Re and Re$_M$ are given for the saturated state.

3.1. Dynamos without shear

For all the cases in Table 1, there is dynamo action. The resulting magnetic field has spatio-temporal coherence with a systematic large-scale magnetic field oscillation on a time scale long compared with the turnover time of the turbulence. As noted above, however, although B_{rms} is seen to increase with increasing magnetic Reynolds number, Re$_M$ = Pr$_M$Re, the rms magnetic field contained in the mean field, $\overline{B}_{rms}$, is seen to decrease.

In Figure 2, we show zt diagrams, also known as butterfly diagrams, for the two relevant components of $\overline{\boldsymbol{B}}$ for Run D with Pr$_M$ = 10. We see migration of the magnetic field away from the boundaries at $k_1 z_\pm = \pm\pi$. This is expected for α^2 dynamos with a non-uniform distribution of α (Stefani & Gerbeth 2003; Cole et al. 2016), or even for a uniform α, but with different boundary conditions on two opposite ends; see Brandenburg (2017).

### 3.2. Turbulent transport coefficients

To identify the nature of the large-scale dynamo seen above, it is useful to compute the turbulent transport coefficients for the horizontal averages applied in this study. All our test-field runs have $\nu = 5 \times 10^{-4} c_s/k_1$. We adopt the expansion $\eta_t = \sum_{\ell=0}^3 \eta_t^{(\ell)} P_\ell(\cos k_1 z)$. In the range $k_1|z| \leq 2.5$, we determine a linear fit to $C_\alpha(z) \approx \alpha/\eta_t k_1$. For larger values of $|z|$, C_α varies no longer linearly, so this part is ignored in the fit.

In Figure 3, we show time-averaged profiles of $\alpha(z)$, $\gamma(z)$, $\eta_t(z)$, and $\delta(z)$ for Run D with Pr$_M$ = 10. For normalization purposes, we adopt the following estimates for the α effect and the turbulent magnetic diffusivity:

$$\alpha_0 = -\epsilon_{f0} u_{rms}/3, \quad \eta_{t0} = u_{rms}/3k_f. \qquad (19)$$
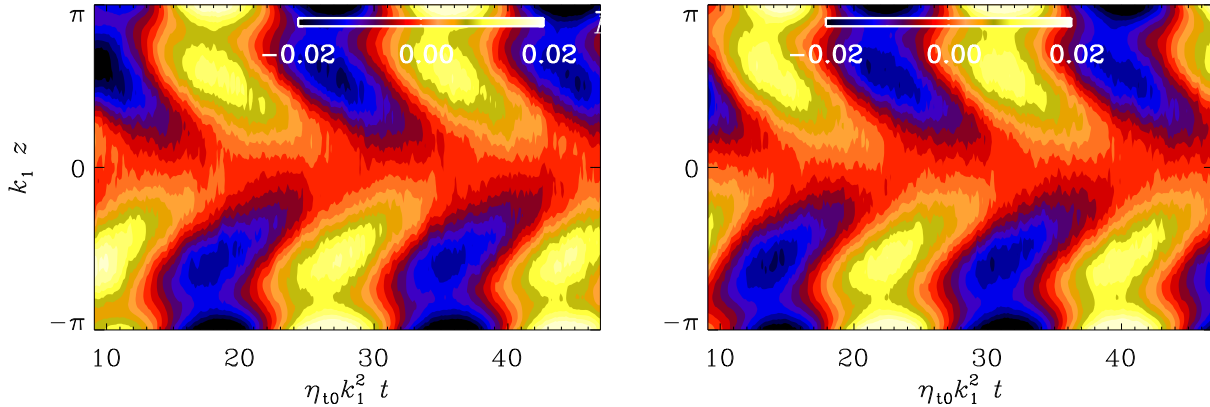
Figure 2. Butterfly diagrams for $\overline{B}_x$ (left) and $\overline{B}_y$ (right) for Run D with $\mathrm{Pr_M} = 10$. $\mathrm{Pr_M} = 10$, $\eta = 5 \times 10^{-5}$, $\nu = 5 \times 10^{-4}$.
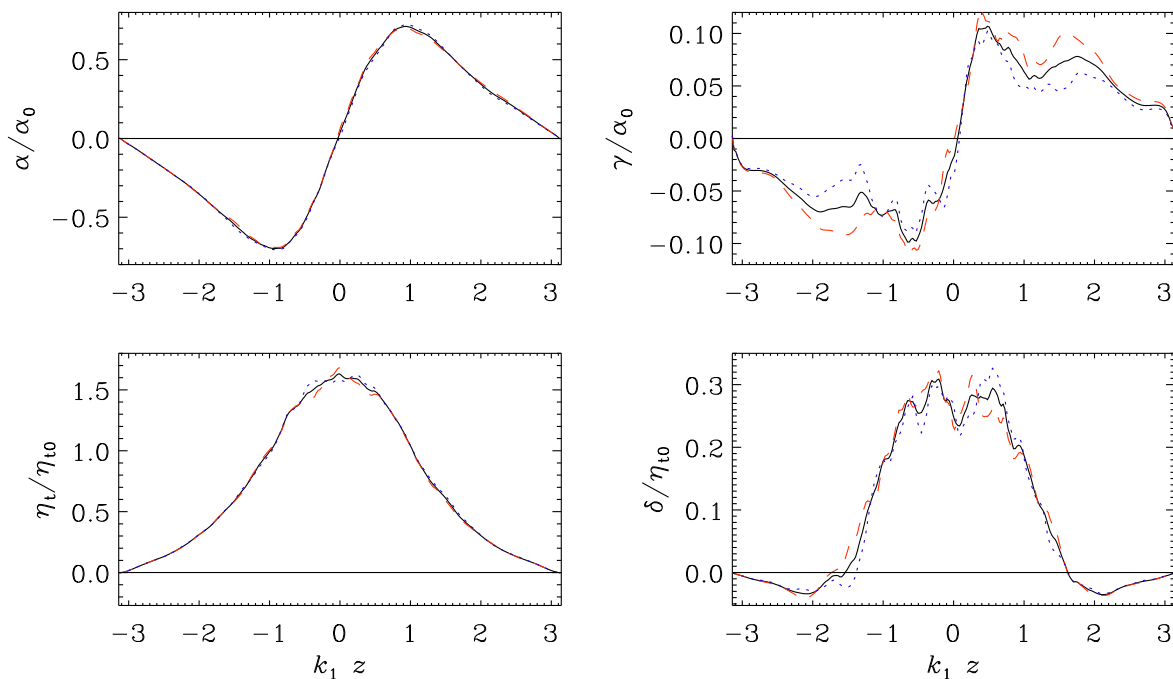
Figure 3. The black lines denote the time-averaged normalized profiles of α, γ, η_t, and δ for Run D with $\mathrm{Pr_M} = 10$, $\eta = 5 \times 10^{-5}$, $\nu = 5 \times 10^{-4}$. In the four panels, the red (blue) lines denote α_{xx} (α_{yy}), α_{yx} ($-\alpha_{xy}$), η_{xx} (η_{yy}), and η_{xy} ($-\eta_{yx}$). The ratio, $\alpha/\eta_\mathrm{t} k_1$, shows local extrema at $k_1 z = \pm 2$ of about 5, but has here a nearly linear profile as a function of z.

Note that in all our simulations (both with and without shear) α_0 is negative. In Figure 3, the ratio $\alpha/\eta_\mathrm{t} k_1$ shows local extrema at $k_1 z = \pm 2$ of about ± 5, but has here a more linear profile as a function of z than for Run A. The profile $\gamma(z)$ quantifies turbulent pumping. It is negative in the southern hemisphere and positive in the northern hemisphere. Since $\boldsymbol{\gamma}$ play the role of an advection vector (albeit without any material motion), this corresponds to magnetic field pumping away from the midplane; see Shukurov & Subramanian (2022) for a review. The profile $\delta(z)$ describes the $\boldsymbol{\Omega} \times \overline{\boldsymbol{J}}$ or Rädler effect (Rädler 1969), which is known to contribute to dynamo action, although this term alone cannot contribute

to a change in $\overline{\boldsymbol{B}}^2$. The sign of δ is here as expected from theory, and it also agrees with earlier test-field results (Brandenburg et al. 2008a).

For the corresponding results for Run A with $\mathrm{Pr_M} = 0.2$, the ratio $\alpha/\eta_\mathrm{t} k_1$, again, shows local extrema at $k_1 z = \pm 2$ of about ± 5.

3.3. *Importance of mean-field effects*

To assess the relative importance of the turbulent transport coefficients, we have solved the relevant mean-field model with Equation (10) using the coefficient from Run D. We find that the model with all the mean-field transport coefficients included yields a slow growth with

Table 2. Growth rates λ for mean-field models for different combinations of c_γ and c_δ using the test-field results for Run D, Run D with shear, and Run E with shear. In the last row, the factor c_α by which α needs to be scaled to reach a marginally excited state, is given for Run D.

			. . . . $\lambda/c_\mathrm{s}k_1$		
c_α	c_γ	c_δ	Run D	Run D+Sh	Run E+Sh
1	1	1	0.0021	0.023	0.0051
1	0	1	0.0017	0.021	0.0046
1	1	0	0.0022	0.021	0.0054
1	0	0	0.0020	0.020	0.0050
0.25	0	0	0	...	...

the growth rate $\lambda/c_\mathrm{s}k_1 = 0.0021$. The fact that this number is different from zero, even though the original direct numerical simulation has reached a steady state, remains unexplained. To reach a marginally excited state, we would need to scale down the α tensor by a factor of about four to reach a marginally excited state. Similar departures from the expected vanishing growth rate have been seen before; see Warnecke et al. (2021) for simulations in spherical geometry, where the α tensor needed to be scaled up to reach a marginally excited state.

We now study the relative importance of the off-diagonal terms of both the α_{ij} and η_{ij} tensors. In Table 2, we give the values of λ after having rescaled the off-diagonal components of the two tensors by scaling coefficients

$$\alpha_{ij} \to c_\gamma\,\alpha_{ij}, \quad \eta_{ij} \to c_\delta\,\eta_{ij}, \quad i \neq j. \tag{20}$$

Thus, when $c_\gamma = 0$ (1), the γ effect is ignored (included), and when $c_\delta = 0$ (1), the δ effect is ignored (included). For Run D, we also have shown the factor $c_\alpha = 0.25$ by which α needs to be scaled to reach a marginally excited state. We also studied models in which we included spatiotemporal nonlocality by solving a differential equation for $\overline{\mathcal{E}}$ (Rheinhardt & Brandenburg 2012; Brandenburg & Chatterjee 2018; Pipin 2023), but this did not change the value of c_α significantly.

From the results presented in Table 2, we see that ignoring the γ effect for the profiles from Run D (Figure 3), decreases the growth rate slightly. Thus, the inclusion of the γ effect supports dynamo action in our case. On the other hand, ignoring the δ effect increases the growth rate slightly. Therefore, the inclusion of the δ effect suppresses dynamo action slightly. On the other hand, the changes in the growth rate are surprisingly small, so it is probably reasonable to say that the importance of the off-diagonal components in the model

is small and that the dynamo is well described by an isotropic α^2 dynamo.

Next, we add shear of the same strength as for Run E (Table 2), but we continue using the mean-field transport profiles of Run D (Figure 3). This is obviously inconsistent, but it allows us to isolate the effect of shear in the mean-field model from that of the profiles for α_{ij} and η_{ij}. The overall growth rate is about ten times larger than without shear, but the differences in the growth rates for different combinations of c_γ and c_δ are small. In summary, we find that both the γ effect and the δ effect contribute slightly to dynamo action, and that excluding them decreases the growth rate slightly.

On the other hand, when one uses the actual profiles for Run E together with shear, we find not only larger differences for different combinations of c_γ and c_δ, but the overall grow rates are also decreased by a factor of about 4 and are now only about 2.5 times larger than for the profiles of Run D and no shear. In particular, the inclusion of the δ and shear–current effects supports dynamo action while the inclusion of the γ effect diminishes dynamo action. In units of $u_\mathrm{rms}k_\mathrm{f}$, the value $\lambda/c_\mathrm{s}k_1$ corresponds to $\lambda/u_\mathrm{rms}k_\mathrm{f} = 0.01$.

### 3.4. *Interpretation of magnetic helicity fluxes*

We are interested in the magnetic helicity flux between the northern and southern hemispheres. It is convenient to plot the magnetic helicity flux through any xy plane as a function of z. In Figure 4, we see that for Run D, most of the total magnetic helicity flux is contained in the large-scale contribution, $\overline{\boldsymbol{E}} \times \overline{\boldsymbol{A}}$. The small-scale magnetic helicity flux is nearly negligible. The large-scale component is nearly balanced by the fluxes $2\int_{-\pi}^{0} \overline{\boldsymbol{\mathcal{E}}} \cdot \overline{\boldsymbol{B}}\,\mathrm{d}z$ and $2\int_{0}^{\pi} \overline{\boldsymbol{\mathcal{E}}} \cdot \overline{\boldsymbol{B}}\,\mathrm{d}z$ between different scales in the southern and northern hemispheres. At small scales, however, almost the entire flux is absorbed by the Ohmic diffusion term $2\eta\mu_0\overline{\boldsymbol{j} \cdot \boldsymbol{b}}$, which was also found for most of the earlier work (Del Sordo et al. 2013; Rincon 2021), when Re_M was not yet very large.

For the much more diffusive Run A with $\mathrm{Pr}_\mathrm{M} = 0.2$, the situation is a bit different; see Figure 5. Here, the integrated $2\overline{\boldsymbol{\mathcal{E}}} \cdot \overline{\boldsymbol{B}}$ term is still balanced by the integrated $-2\eta\mu_0\overline{\boldsymbol{j} \cdot \boldsymbol{b}}$ term, but now there is also a significant contribution from the integrated $2\eta\mu_0\overline{\boldsymbol{J}} \cdot \overline{\boldsymbol{B}}$ term, which balances $\overline{\boldsymbol{E}} \times \overline{\boldsymbol{A}}$. Looking at Figure 1, this means that the microphysical magnetic diffusivity is important not only at small scales, when the integrated $2\overline{\boldsymbol{\mathcal{E}}} \cdot \overline{\boldsymbol{B}}$ term is entirely supplied by the integrated $-2\eta\mu_0\overline{\boldsymbol{j} \cdot \boldsymbol{b}}$ term and not much by the $\overline{\boldsymbol{e} \times \boldsymbol{a}}$ or integrated $\overline{\phi\boldsymbol{b}}$ terms, but also at large scales, when the integrated $2\overline{\boldsymbol{\mathcal{E}}} \cdot \overline{\boldsymbol{B}}$ term is supplied to 50% by the integrated $\eta\nu_0\overline{\boldsymbol{J} \cdot \boldsymbol{B}}$ term and to another 50% by $\overline{\boldsymbol{E} \times \boldsymbol{A}}$.
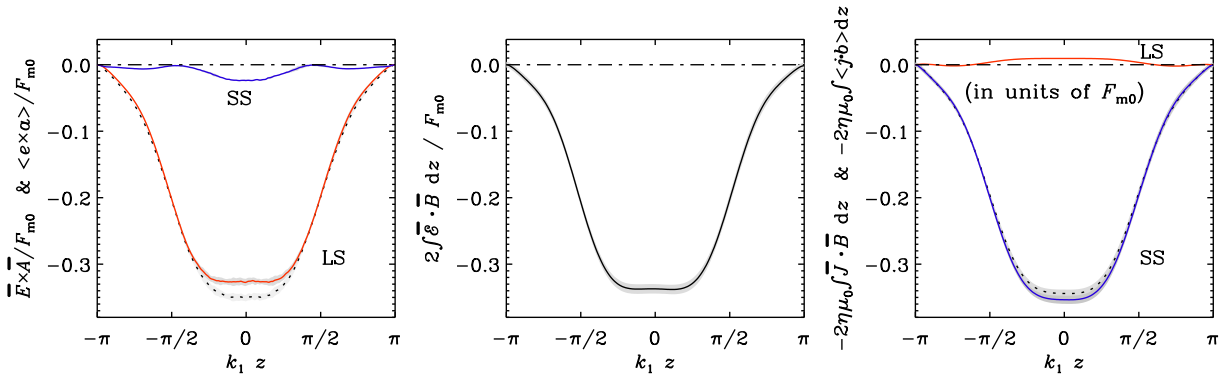
Figure 4. Magnetic helicity fluxes for Run D with $Pr_M = 10$. $\eta = 5 \times 10^{-5}$, $\nu = 5 \times 10^{-4}$. The blue (red) lines denote the small-scale (large-scale) contributions, where applicable, and the black dotted lines denote their sum. The black dashed-dotted line is the zero line. Note that the $\overline{\boldsymbol{j} \cdot \boldsymbol{b}}$ and $\overline{\boldsymbol{J} \cdot \boldsymbol{B}}$ terms have been plotted with a minus sign, so $2\eta\mu_0 \int \overline{\boldsymbol{j} \cdot \boldsymbol{b}} \, dz$ is here positive.
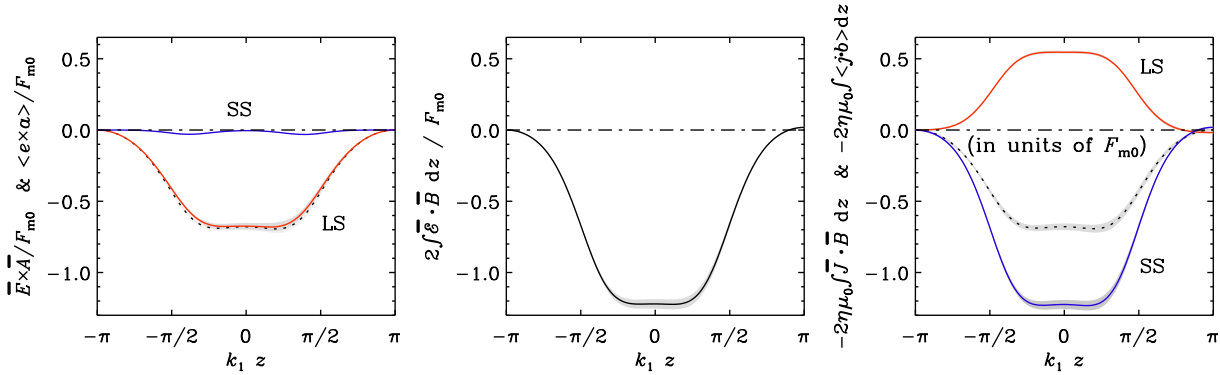
Figure 5. Similar to Figure 4, but for Run A with $Pr_M = 0.2$. $\eta = 2.5 \times 10^{-3}$, $\nu = 5 \times 10^{-4}$. Note that the integrated $2\overline{\boldsymbol{\mathcal{E}}} \cdot \overline{\boldsymbol{B}}$ term is balanced by the integrated $-2\eta\mu_0\overline{\boldsymbol{j} \cdot \boldsymbol{b}}$ term, but there is also a significant contribution from the integrated $2\eta\mu_0\overline{\boldsymbol{J}} \cdot \overline{\boldsymbol{B}}$ term, which balances $\overline{\boldsymbol{E}} \times \overline{\boldsymbol{A}}$.

Table 3. The contributions from $F_{m0}^{-1}(\overline{\boldsymbol{e} \times \boldsymbol{a}})_z$, $2F_{m0}^{-1} \int \overline{\boldsymbol{\mathcal{E}}} \cdot \overline{\boldsymbol{B}} \, dz$, and $-2\eta\mu_0 F_{m0}^{-1} \int \overline{\boldsymbol{j} \cdot \boldsymbol{b} \, dz}$ to the magnetic helicity flux balance, along with other properties, for runs with shear.

Run	Re	Re$_M$	Pr$_M$	$\eta k_1/c_s$	$F_{m0}^{-1} \times$ $(\overline{\boldsymbol{e} \times \boldsymbol{a}})_z$	$-2F_{m0}^{-1} \times$ $\int \overline{\boldsymbol{\mathcal{E}}} \cdot \overline{\boldsymbol{B}} \, dz$	$-2\eta\mu_0 F_{m0}^{-1} \times$ $\int \overline{\boldsymbol{j} \cdot \boldsymbol{b}} \, dz$	$-\epsilon_{f0}$	ϵ_{f0}^M	k_{eff}	— $B_{eq}^{-1} \times$ — B_{rms}	$\overline{B}_{rms}$	N^3
E	12.3	123	10	5×10^{-5}	0.035	0.035	0.005	0.22	0.007	3.0	1.39	0.34	256^3
F	12.9	258	20	2.5×10^{-5}	0.045	0.015	0.030	0.22	0.05	15	1.58	0.31	512^3
G	13.2	660	50	10^{-5}	0.025	0.005	0.020	0.15	0.10	24	2.62	0.37	1024^3
H	160	160	1	5×10^{-5}	0.075	0.160	-0.085	0.33	-0.02	14i	0.94	0.22	512^3
I	340	340	1	2×10^{-5}	0.060	0.040	0.020	0.26	0.04	16	1.10	0.28	512^3
J	540	540	1	10^{-5}	0.075	0.020	0.055	0.16	0.10	16	1.24	0.24	512^3
K	850	850	1	5×10^{-6}	0.060	0.015	0.045	0.08	0.07	17	1.24	0.21	512^3
L	410	164	0.4	5×10^{-5}	0.050	0.130	-0.080	0.33	-0.03	9i	0.94	0.22	512^3
M	830	166	0.2	5×10^{-5}	0.075	0.075	-0.000	0.33	-0.00	3	0.91	0.20	512^3
N	1650	165	0.1	5×10^{-5}	0.060	0.140	-0.080	0.33	-0.03	13i	0.92	0.25	512^3
O	690	345	0.5	2×10^{-5}	0.120	0.020	0.100	0.26	$+0.07$	12	1.05	0.18	512^3
P	1700	340	0.2	2×10^{-5}	0.070	0.050	0.020	0.25	$+0.04$	13	1.08	0.26	512^3

3.5. *The effect of shear*

We now consider models with finite shear using $q = 0.5$ (so $V_y = -q\Omega x$). This value is less than what is used to model Keplerian shear, where $q = 3/2$. As emphasized above, this is because we want to avoid supersonic speeds on the shearing boundaries at $x = \pm\pi$. In the
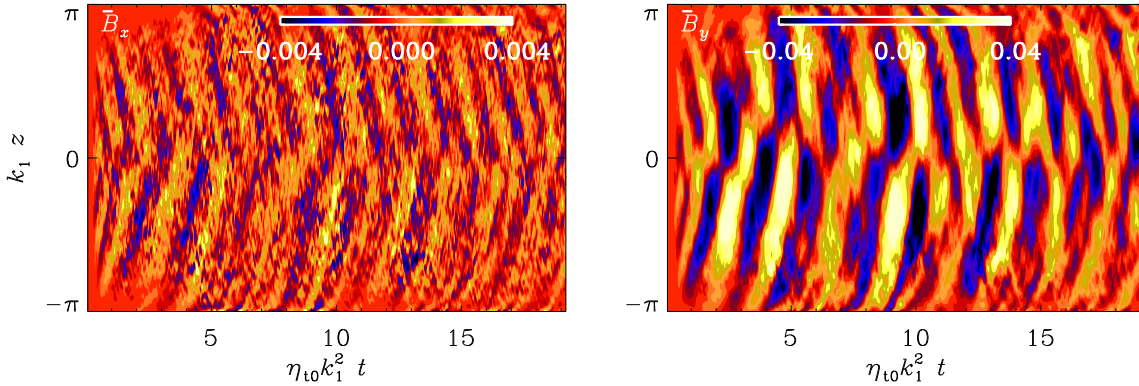
Figure 6. Butterfly diagrams for $\overline{B}_x$ (left) and $\overline{B}_y$ (right) for Run E with shear and $\mathrm{Pr}_M = 10$.
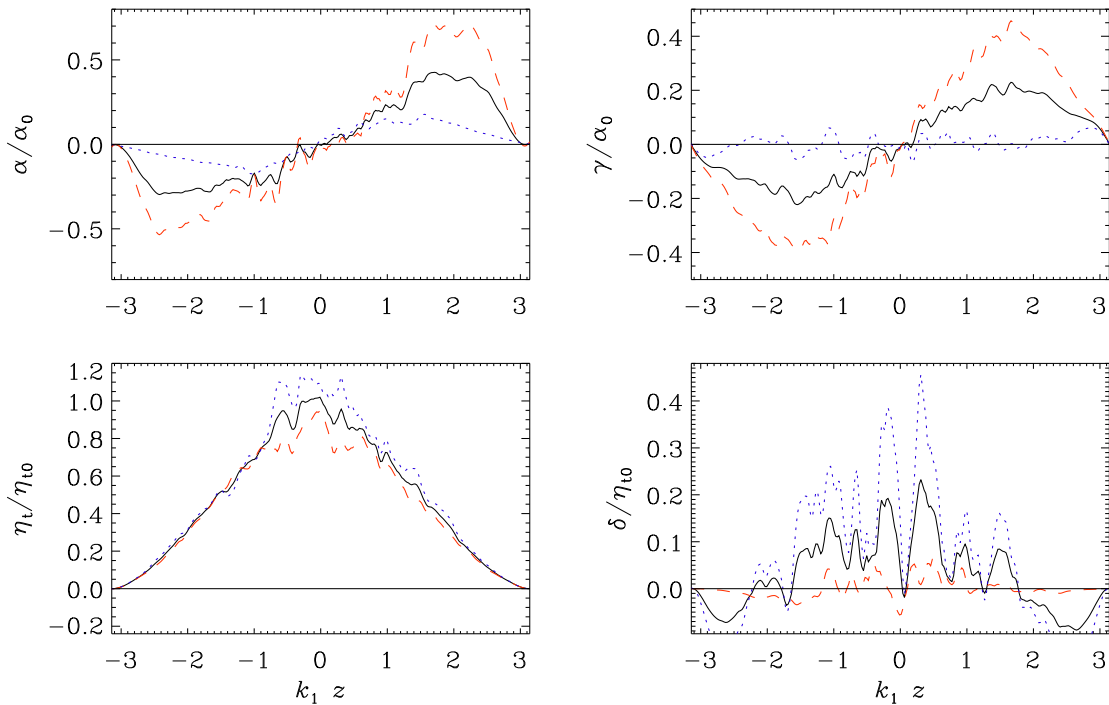

Figure 7. Time-averaged profiles of α, γ, η_t, and δ for Run E with shear and $\mathrm{Pr}_M = 10$. The ratio, $\alpha/\eta_t k_1$, shows local extrema at $k_1 z = \pm 2$ of about 5, but has here a more linear profile as a function of z. The red lines refer to $\alpha_{xx}(z)$, $\alpha_{yx}(z)$, $\eta_{xx}(z)$, $\eta_{yx}(z)$, and the blue lines to $\alpha_{yy}(z)$, $\alpha_{xy}(z)$, $\eta_{yy}(z)$, and $\eta_{xy}(z)$. Note that, while $\eta_{xx} \approx \eta_{yy}$, we find that $\alpha_{xx} \gg \alpha_{yy}$. Also, $\alpha_{yx} \gg \alpha_{xy}$, i.e., the pumping of $\overline{B}_x$ is stronger than that of $\overline{B}_y$.

present case with $\Omega/c_s k_1 = 0.5$ and $q = 0.5$, we have $V_y(\pm\pi) = \mp 0.8 c_s$. Run E is an example of a model with shear. The fluxes for this and a few other runs with shear are summarized in Table 3. In Figure 6, we show butterfly diagrams for $\overline{B}_x$ and $\overline{B}_y$ for Run E with shear and $\mathrm{Pr}_M = 10$. They are consistent with earlier results by Stepinski & Levy (1990), where the field is confined to the disc, which is here accomplished by the use of perfect conductor boundary conditions; see Brandenburg & Campbell (1997) for further detail and references. Similarly to the cases without shear, as we increase the value of Pr_M further and Re_M increases,

the ratio $B_{\mathrm{rms}}/B_{\mathrm{eq}}$ increases, but now the level of the mean field, $\overline{B}_{\mathrm{rms}}/B_{\mathrm{eq}}$, stays approximately the same. This might suggest that catastrophic quenching is now alleviated.

In Figure 7, we show time-averaged profiles of α, γ, η_t, and δ for Run E. We see that, while $\eta_{xx} \approx \eta_{yy}$, we find that $\alpha_{xx} \gg \alpha_{yy}$. This agrees with earlier simulations of Brandenburg (2005), but is opposite to the results of Gressel et al. (2008). Furthermore, we find that $\alpha_{yx} \gg \alpha_{xy}$, i.e., the pumping of $\overline{B}_x$ is stronger than that of $\overline{B}_y$; see Ossendrijver et al. (2002) for earlier work on
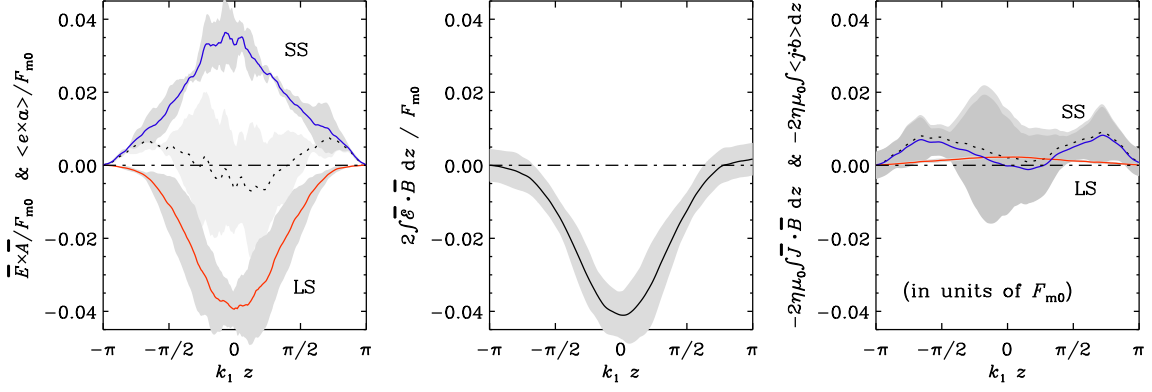
Figure 8. Similar to Figure 4, but for Run E with shear and $Pr_M = 10$. Large-scale and small-scale magnetic helicity fluxes nearly cancel. In the small-scale magnetic helicity equation, the integrated $2\overline{\mathcal{E}} \cdot \overline{B}$ term balances $\overline{e \times a}$, and the integrated $-2\eta \overline{j \cdot b}$ term is small. We recall that the $\overline{j \cdot b}$ and $\overline{J} \cdot \overline{B}$ terms have been plotted with a minus sign, so $2\eta\mu_0 \int \overline{j \cdot b} \, dz$ is now negative.
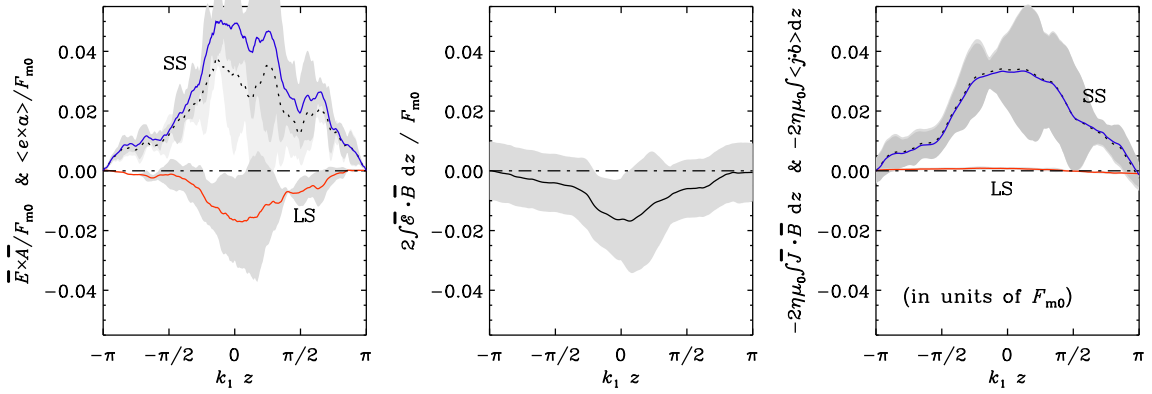
Figure 9. Similar to Figure 8, but for Run F with $Pr_M = 20$.

directionally dependent pumpings of the magnetic field in a sphere.

The contribution from η_{xy} is rather small and, as already emphasized before, that from η_{yx} fluctuates around zero. It is this component that is relevant for the shear–current effect (Rogachevskii & Kleeorin 2003, 2004). Its magnetic contribution to the shear–current effect was thought to be an important driver (Squire & Bhattacharjee 2015), but even the fully nonlinear test-field method did not show such a contribution (Käpylä et al. 2020).

In Figure 8, we show magnetic helicity fluxes for Run E. Large-scale and small-scale magnetic helicity fluxes nearly cancel and are nearly equally important. It is striking to note that the small-scale magnetic helicity flux, arising from the correlated action of the turbulent eddies, roughly scales as the turbulent energy density and has the same sign throughout the computational volume. In the third panel of Figure 8, we see the integrated small-scale current helicity, which oscillates from zero to a negative maximum back to zero twice. This implies that the current helicity, and the associ-

ated magnetic helicity, oscillates through two full cycles within the computational volume. The small-scale magnetic helicity flux seen in the first panel shows a negligible contribution from the turbulent diffusion term of the form $-\kappa_t \nabla_z h$, where κ_t is a turbulent diffusivity and $h = \overline{a \cdot b}$ is the small-scale magnetic helicity density.

In Equation (13) for the large-scale helicity equation, the integrated $2\overline{\mathcal{E}} \cdot \overline{B}$ term balances $\overline{E} \times \overline{A}$, and in Equation (14), also $\overline{e \times a}$ balances $2 \int \overline{\mathcal{E}} \cdot \overline{B} \, dz$, so, contrary to the cases without shear, the integrated $2\eta\mu_0 \overline{j \cdot b}$ term is small, and the integrated $2\eta\mu_0 \overline{J} \cdot \overline{B}$ term is smaller still. This was not the case in much of the earlier work without shear (Del Sordo et al. 2013; Rincon 2021).

For Run F, $\overline{E} \times \overline{A}$ stays unchanged, but $2 \int \overline{\mathcal{E}} \cdot \overline{B} \, dz$ now decreases and $2\eta\mu_0 \int \overline{j \cdot b} \, dz$ increases and is of opposite sign compared to before; see Figure 9. This trend persists even for Run G, although here the statistical significance is more questionable; see Figure 10.

The Re_M-dependence of the magnetic helicity fluxes in Table 3 is unexpected. This dependence is shown more clearly for Runs E–G and Runs H–K in Figure 11, where $-2 \int \overline{\mathcal{E}} \cdot \overline{B} \, dz$ displays a monotonic decrease proportional
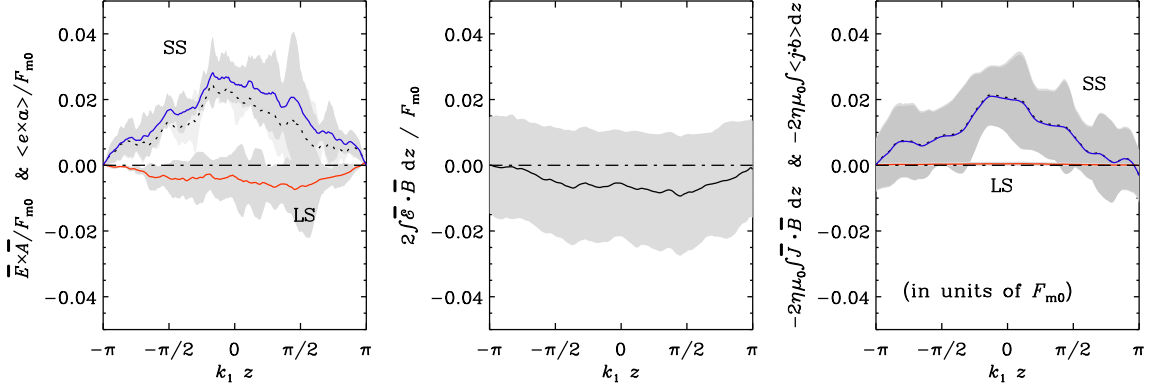
Figure 10. Similar to Figure 9, but for Run G with $\mathrm{Pr_M} = 50$.
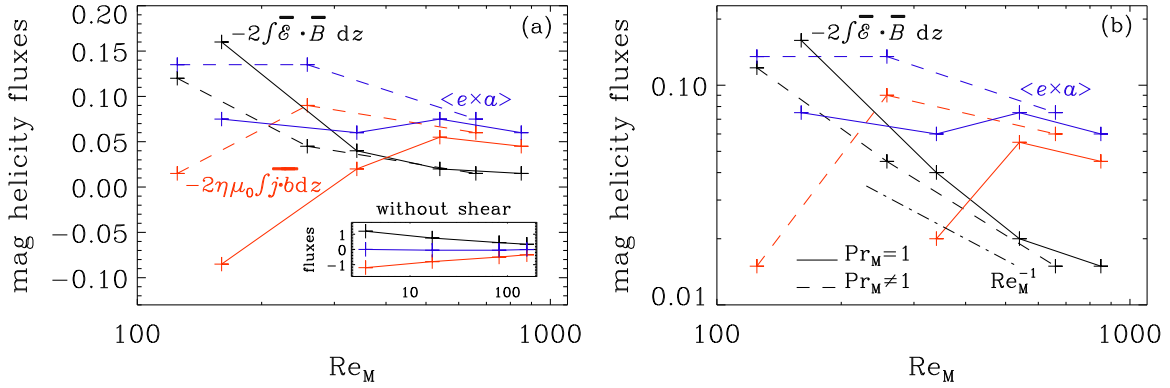
Figure 11. Summary of the small-scale magnetic helicity fluxes (blue line) and the typical values of $-2\int \overline{\boldsymbol{\mathcal{E}}} \cdot \overline{\boldsymbol{B}}\,\mathrm{d}z$ (black lines) and $-2\eta\mu_0 \int \overline{\boldsymbol{j}\cdot\boldsymbol{b}}\,\mathrm{d}z$ (red lines) for the runs with shear in semi-logarithmic (a) and double-logarithmic (b) representations. The latter also shows the $\mathrm{Re_M^{-1}}$ scaling as the dashed-dotted line. The dashed lines connecting each three data points are for Runs E–G (with $\mathrm{Pr_M} \neq 1$) and the solid lines for Runs H–K (with $\mathrm{Pr_M} = 1$). The lines for Runs E–G have been upscaled by a factor 3 to make them coincide with those for Runs H and I. The inset shows the fluxes for Runs A–D without shear in the same color coding.

to $\mathrm{Re_M^{-1}}$. The small-scale magnetic helicity flux divergence, on the other hand, is nearly constant in all cases and strongly exceeds $-2\int \overline{\boldsymbol{\mathcal{E}}} \cdot \overline{\boldsymbol{B}}\,\mathrm{d}z$ for large values of $\mathrm{Re_M}$. As a consequence, to obey the steady-state condition of Equation (14), the magnetic helicity dissipation must become important at large $\mathrm{Re_M}$. A similar behavior has not previously been seen in the absence of shear; see the corresponding plots of Del Sordo et al. (2013) and Rincon (2021) and the inset to Figure 11. Looking again at Table 3, we see, however, that the integrated $\overline{\boldsymbol{j}\cdot\boldsymbol{b}}$ terms do still obey Equation (16), i.e.,

$$\overline{\boldsymbol{e}\times\boldsymbol{a}} = -2\int_{z_-}^{z}\left(\overline{\boldsymbol{\mathcal{E}}} \cdot \overline{\boldsymbol{B}} + \eta\mu_0\overline{\boldsymbol{j}\cdot\boldsymbol{b}}\right)\,\mathrm{d}z. \qquad (21)$$

We have seen that for larger values of $\mathrm{Pr_M}$ and $\mathrm{Re_M}$, the small-scale magnetic helicity flux, $\overline{\boldsymbol{e}\times\boldsymbol{a}}$, stays approximately unchanged, although the integrated $-2\overline{\boldsymbol{\mathcal{E}}}\cdot\overline{\boldsymbol{B}}$ term still declines with larger values of $\mathrm{Re_M}$. Thus, there is now an excess of small-scale magnetic flux from south to north. This excess must be dissipated by the inte-

grated Ohmic term $2\eta\mu_0\overline{\boldsymbol{j}\cdot\boldsymbol{b}}$. Such a behavior is rather unexpected and it seems to be a general consequence of dynamos with shear and large values of $\mathrm{Re_M}$, and is not just a specific consequence of large values of $\mathrm{Pr_M}$.

3.6. Super-equipartition with shear

The reason why our runs with shear show strong small-scale magnetic helicity fluxes is probably connected with the fact that in those runs, the magnetic field reaches super-equipartition strengths. This is seen in Table 3, where $B_{\mathrm{rms}}/B_{\mathrm{eq}} > 1$, and in Figure 12, where we plot for Run E the temporal evolution of $\langle\boldsymbol{B}^2\rangle$, $B_{\mathrm{eq}}^2 = \mu_0\rho_0\,u_{\mathrm{rms}}^2$, $\langle B_y^2\rangle$, and $\langle B_x^2\rangle$. We see that the total (small-scale and large-scale) magnetic field reaches super-equipartition field strengths at $t \approx 300/c_s k_1$, which is clearly before the large-scale magnetic field saturates at $t \approx 1000/c_s k_1$, which is when $\langle B_y^2\rangle$ has reached a statistically steady state. Interestingly, the large-scale magnetic field displays an approximately exponential growth at a rate $10^{-2}\,u_{\mathrm{rms}}k_{\mathrm{f}}$ for the squared mean-field
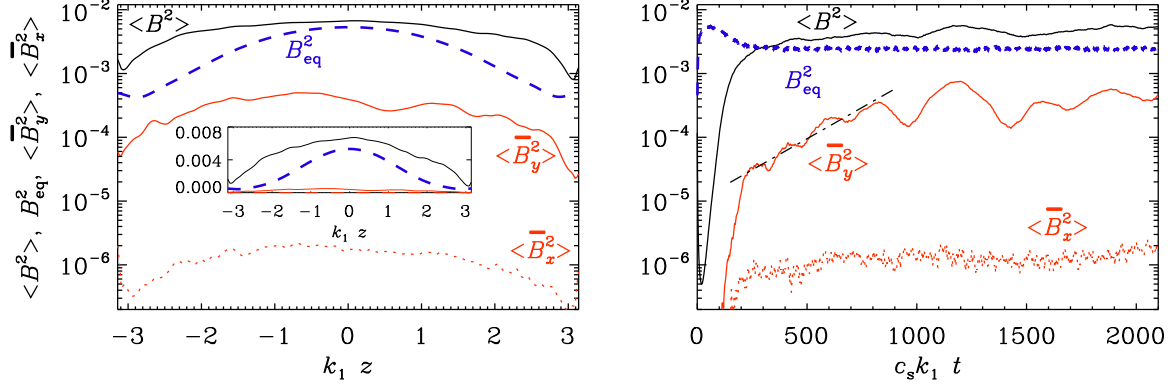
Figure 12. (a) z-profiles of $\langle \boldsymbol{B}^2 \rangle_{xyt}$ (solid black), B_{eq}^2 (dashed blue), $\langle \overline{B}_y^2 \rangle_t$ (solid red), and $\langle \overline{B}_x^2 \rangle_t$ (dotted red). (b) t-profiles of $\langle \boldsymbol{B}^2 \rangle_{xyz}$ (solid black), B_{eq}^2 (dashed blue), $\langle \overline{B}_y^2 \rangle_z$ (solid red), and $\langle \overline{B}_x^2 \rangle_z$ (dotted red) for Run E, here plotted in code units, $[B] = \mu_0 \rho_0 c_{\mathrm{s}}^2$. The dashed-dotted line indicates a slow, but exponential growth with the growth rate $10^{-2}\, u_{\mathrm{rms}} k_{\mathrm{f}}$, for the squared mean-field strength.
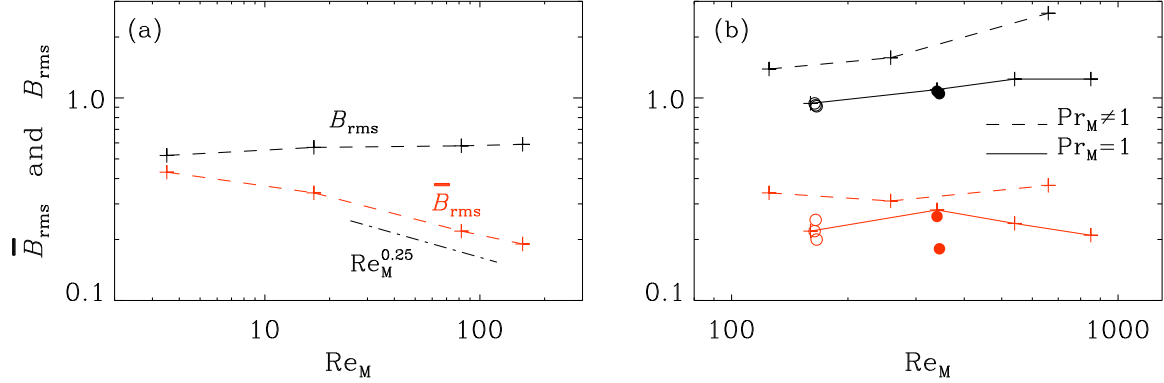
Figure 13. Dependence of B_{rms} (black) and $\overline{B}_{\mathrm{rms}}$ (red) on Re_{M} (a) without shear and (b) with shear. Dashed lines indicate that Re_{M} is varied by changing Pr_{M} [Runs A–D in (a) and Runs E–G in (b)], while solid lines indicate that Re has been changed [Runs H–K in (b)]. In (b), the open and closed circles are for Runs L–N and O+P, respectively.

strength. The growth rate of the mean field is then half that value, which is comparable to the growth rates found in Table 2, where $\lambda/c_{\mathrm{s}} k_1 \approx 0.005$, corresponding to $\lambda/u_{\mathrm{rms}} k_{\mathrm{f}} \approx 0.01$.

In the shear-induced super-equipartition regime, the rms values of the resulting large-scale magnetic field are found to be independent of Re_{M}. In the absence of shear, $\overline{B}_{\mathrm{rms}}$ clearly declined with Re_{M}, albeit only like $\mathrm{Re}_{\mathrm{M}}^{0.3}$; see Figure 13(a). With shear, however, $\overline{B}_{\mathrm{rms}}$ is nearly independent of Re_{M}; see Figure 13(b). The fact that resistive contributions through the integrated $2\eta\mu_0 \overline{\boldsymbol{j} \cdot \boldsymbol{b}}$ term become increasingly important can be regarded as a consequence of the shear-induced hemispheric magnetic helicity fluxes that become extremely efficient at exchanging small-scale magnetic helicity between hemispheres. We can therefore say that they overcome catastrophic quenching so as to guarantee an Re_{M}-independent large-scale magnetic field.

The strong contribution of the small-scale current helicity term might raise concerns whether the simulation

is sufficiently well resolved. To check this, we plot in Figure 14 an xy slice of J_x through $k_1 z = 1$, but no signs of ringing, i.e., no oscillations on the grid scale are seen. Instead, it shows the typical inclined patterns associated with the shear flow, $\overline{U}_y(x) = -q\Omega x$.

In Figure 15, we present kinetic and magnetic energy spectra for Runs G and K. Both runs have shear, but different values of Pr_{M}. The spectra are similar, except that the magnetic and velocity spectra for Run K have still more energy at the largest wavenumber of the mesh, i.e., at the Nyquist wavenumber $k_1 N/2$.

4. CONCLUSIONS

In this paper we have considered a volume containing a modulated level of turbulence, which drops to zero at the vertical boundaries, so that the internal transport coefficients of the medium go to zero smoothly at those boundaries. Consequently, the results of the simulations should be insensitive to the vertical boundary conditions. The properties of the medium, including
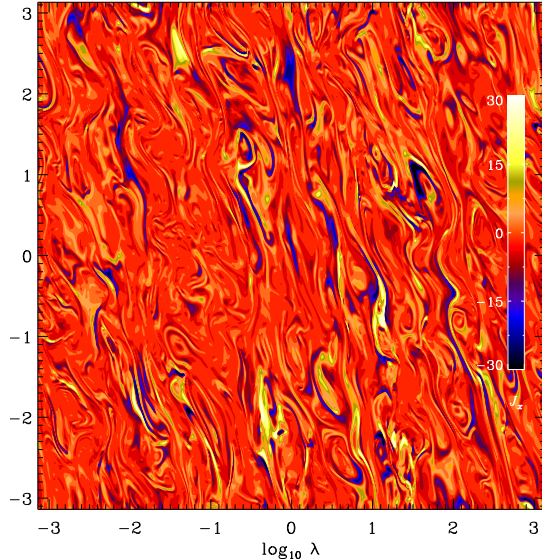
Figure 14. Slice of $J_x(x, y, z_*)$ for Run G at $k_1 z_* = 1$, showing a systematic tilt from the upper left to the lower right, with all structures being well resolved.
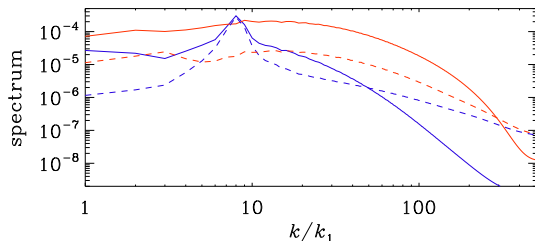
Figure 15. Three-dimensional kinetic (blue) and magnetic (red) energy spectra for Runs G (solid lines) and K (dashed lines).

rotation and shear, are otherwise uniform within the volume.

The existence of a systematic flux of small-scale helicity, as seen in Figure 8, is consistent with a simple dimensional estimate. A magnetic helicity flux arising from turbulence should scale with $\overline{\boldsymbol{u}^2 \boldsymbol{B}^2} \tau$, where τ is a correlation time (Kleeorin & Rogachevskii 2022). However, the magnetic helicity flux is a pseudovector, with a direction, which requires a scaling with either the rotation or the shear (or more particularly with the local vorticity), which implies an extra factor of $\Omega \tau$ or $S \tau$. For a uniform driving scale of the turbulence, and a uniform shear and rotation, we expect a magnetic helicity flux proportional to $\overline{\boldsymbol{B}^2}$, which is consistent with the evidence in case E. Our results suggest that this flux is significantly more sensitive to shear than to rotation.

We have shown that in a large-scale dynamo, the magnetic helicity fluxes between large and small scales can even become overcompensated by those between the two hemispheres when microphysical resistive effects are small. In the absence of shear and at small magnetic Reynolds numbers (Run A, $\mathrm{Re_M} = 3.5$), these fluxes are comparable to the reference flux defined in Equation (17). For Run D with $\mathrm{Re_M} = 160$, the magnetic helicity fluxes are about 30% of the reference flux. However, while the magnetic helicity flux at large scales is large, that at small scales is virtually absent; see Figures 4 and 5. In the presence of shear and for similar values of $\mathrm{Re_M}$ (Run E), the flux drops to 1–5% of the reference flux, but now the fluxes are approximately the same at large and small scales.

The correspondence between the magnetic helicity flux between hemispheres and between scales is not a coincidence. The small-scale flux between hemispheres depends on the total magnetic field strength, although the small- and large-scale magnetic fields contribute to the flux with different coefficients. The flow of magnetic helicity between scales is proportional to the square of the large-scale field. Consequently, the saturation strength of the large-scale field may be set by the magnetic helicity flux between hemispheres.

While the large fraction of small-scale magnetic helicity fluxes in the presence of shear is indicative of alleviating catastrophic quenching, we do not find that the resistive term becomes unimportant at large magnetic Reynolds numbers. This does not a priori mean that such dynamos are not viable in the large $\mathrm{Re_M}$-regime. The fact that $2 \int \overline{\boldsymbol{\mathcal{E}}} \cdot \overline{\boldsymbol{B}} \, \mathrm{d}z \to 0$ in the large magnetic Reynolds number limit was thought to reflect the basic catastrophic quenching problem of large-scale dynamos with helicity. However, while the hemispheric small-scale magnetic helicity flux stays constant as $\mathrm{Re_M}$ increases, it is not being used to balance the integrated $2 \overline{\boldsymbol{\mathcal{E}}} \cdot \overline{\boldsymbol{B}}$ term, but it either drives or is driven by the integrated $2 \eta \mu_0 \overline{\boldsymbol{j} \cdot \boldsymbol{b}}$ term.

Our models have demonstrated that interesting flux dynamics can occur entirely without boundaries. The magnetic helicity fluxes occur within the volume due to gradients of the turbulent intensity and turbulent kinetic and magnetic helicities, as was also found by Kleeorin & Rogachevskii (2022).

Our work has also shown that the dynamos in the present setups are of α^2- or $\alpha\Omega$-type, i.e., they are driven by an α effect and supported by shear, if shear is present. The ratio of the local value of α to the product of the local turbulent magnetic diffusivity and the lowest wavenumber of the domain, i.e., the z-dependent dynamo number, which is found to be an approximately linear function with a coefficient of 2.8 and 2.2 for Runs A and D, respectively. This suggests that the dynamo number decreases with increasing conductiv-

ity. For Run E with shear, the ratio is 1.4. Turbulent pumping points in the direction away from the midplane. There is also a Rädler effect with the theoretically expected sign, i.e., $\overline{\mathcal{E}}$ has a contribution proportional to $\mathbf{\Omega} \times \overline{\mathbf{J}}$ with a positive coefficient. In the presence of shear, the effect becomes anisotropic and the component that is relevant for the shear–current effect, namely the η_{yx} component for shear of the present form $S = \mathrm{d}\overline{U}_y/\mathrm{d}x$, is essentially zero, which is consistent with earlier findings (Brandenburg et al. 2008a; Käpylä et al. 2022).

Our results have applications to stellar and galactic dynamos, where gradients of kinetic and magnetic helicity fluxes are expected to occur through the equator. Even the boundary between convecting and non-convecting regions both in late-type stars and in massive stars are examples, where magnetic helicity fluxes can be expected to encounter dynamical boundaries of the type idealized here.

Software and Data Availability. The source code used for the simulations of this study, the Pencil Code (Pencil Code Collaboration et al. 2021), is freely available on https://github.com/pencil-code/. The simulation setups and corresponding input and reduced out data are freely available on http://norlx65.nordita.org/~brandenb/projects/Omega-Gradu/.

REFERENCES

Armitage, P. J. 2011, ARA&A, 49, 195, doi: 10.1146/annurev-astro-081710-102521

Balbus, S. A., & Hawley, J. F. 1998, Rev. Mod. Phys., 70, 1, doi: 10.1103/RevModPhys.70.1

Beck, R., Brandenburg, A., Moss, D., Shukurov, A., & Sokoloff, D. 1996, ARA&A, 34, 155, doi: 10.1146/annurev.astro.34.1.155

Bermudez, G., & Alexakis, A. 2022, PhRvL, 129, 195101, doi: 10.1103/PhysRevLett.129.195101

Blackman, E. G., & Brandenburg, A. 2002, ApJ, 579, 359, doi: 10.1086/342705

Blackman, E. G., & Field, G. B. 2000, ApJ, 534, 984, doi: 10.1086/308767

Brandenburg, A. 2001, ApJ, 550, 824, doi: 10.1086/319783

—. 2005, Astron. Nachr., 326, 787, doi: 10.1002/asna.200510414

—. 2017, A&A, 598, A117, doi: 10.1051/0004-6361/201630033

—. 2018a, Astron. Nachr., 339, 631, doi: 10.1002/asna.201913604

—. 2018b, J. Plasma Phys., 84, 735840404, doi: 10.1017/S0022377818000806

Brandenburg, A., & Campbell, C. 1997, in Accretion Disks - New Aspects, ed. E. Meyer-Hofmeister & H. Spruit, Vol. 487, 109, doi: 10.1007/BFb0105826

Brandenburg, A., & Chatterjee, P. 2018, Astron. Nachr., 339, 118, doi: 10.1002/asna.201813472

Brandenburg, A., Gressel, O., Käpylä, P. J., et al. 2013, ApJ, 762, 127, doi: 10.1088/0004-637X/762/2/127

Brandenburg, A., Nordlund, A., Stein, R. F., & Torkelsson, U. 1995, ApJ, 446, 741, doi: 10.1086/175831

Brandenburg, A., & Ntormousi, E. 2023, ARA&A, 61, 561, doi: 10.1146/annurev-astro-071221-052807

Brandenburg, A., Rädler, K. H., Rheinhardt, M., & Käpylä, P. J. 2008a, ApJ, 676, 740, doi: 10.1086/527373

Brandenburg, A., Rädler, K.-H., Rheinhardt, M., & Subramanian, K. 2008b, ApJL, 687, L49, doi: 10.1086/593146

Brandenburg, A., Rädler, K. H., & Schrinner, M. 2008c, A&A, 482, 739, doi: 10.1051/0004-6361:200809365

Brandenburg, A., & Scannapieco, E. 2020, ApJ, 889, 55, doi: 10.3847/1538-4357/ab5e7f

Candelaresi, S., Hubbard, A., Brandenburg, A., & Mitra, D. 2011, Phys. Plasmas, 18, 012903, doi: 10.1063/1.3533656

Cattaneo, F., & Hughes, D. W. 1996, PhRvE, 54, R4532, doi: 10.1103/PhysRevE.54.R4532

Charbonneau, P. 2014, ARA&A, 52, 251,
doi: 10.1146/annurev-astro-081913-040012

Cole, E., Brandenburg, A., Käpylä, P. J., & Käpylä, M. J.
2016, A&A, 593, A134,
doi: 10.1051/0004-6361/201628165

Davis, S. W., & Tchekhovskoy, A. 2020, ARA&A, 58, 407,
doi: 10.1146/annurev-astro-081817-051905

Del Sordo, F., Guerrero, G., & Brandenburg, A. 2013,
MNRAS, 429, 1686, doi: 10.1093/mnras/sts398

Field, G. B., & Blackman, E. G. 2002, ApJ, 572, 685,
doi: 10.1086/340233

Gressel, O., Ziegler, U., Elstner, D., & Rüdiger, G. 2008,
Astron. Nachr., 329, 619, doi: 10.1002/asna.200811005

Gruzinov, A. V., & Diamond, P. H. 1996, Phys. Plasmas, 3,
1853, doi: 10.1063/1.871981

Haugen, N. E., Brandenburg, A., & Dobler, W. 2004,
PhRvE, 70, 016308, doi: 10.1103/PhysRevE.70.016308

Hubbard, A., & Brandenburg, A. 2009, ApJ, 706, 712,
doi: 10.1088/0004-637X/706/1/712

—. 2010, GApFD, 104, 577,
doi: 10.1080/03091929.2010.506438

—. 2011, ApJ, 727, 11, doi: 10.1088/0004-637X/727/1/11

—. 2012, ApJ, 748, 51, doi: 10.1088/0004-637X/748/1/51

Jabbari, S., Brandenburg, A., Losada, I. R., Kleeorin, N., &
Rogachevskii, I. 2014, A&A, 568, A112,
doi: 10.1051/0004-6361/201423499

Ji, H. 1999, PhRvL, 83, 3198,
doi: 10.1103/PhysRevLett.83.3198

Jiang, Y.-F., Stone, J. M., & Davis, S. W. 2014, ApJ, 796,
106, doi: 10.1088/0004-637X/796/2/106

Käpylä, M. J., Rheinhardt, M., & Brandenburg, A. 2022,
ApJ, 932, 8, doi: 10.3847/1538-4357/ac5b78

Käpylä, M. J., Vizoso, J. Á., Rheinhardt, M., Brandenburg,
A., & Singh, N. K. 2020, ApJ, 905, 179,
doi: 10.3847/1538-4357/abc1e8

Karak, B. B., Rheinhardt, M., Brandenburg, A., Käpylä,
P. J., & Käpylä, M. J. 2014, ApJ, 795, 16,
doi: 10.1088/0004-637X/795/1/16

Kleeorin, N., Moss, D., Rogachevskii, I., & Sokoloff, D.
2000, A&A, 361, L5,
doi: 10.48550/arXiv.astro-ph/0205266

Kleeorin, N., & Rogachevskii, I. 2022, MNRAS, 515, 5437,
doi: 10.1093/mnras/stac2141

Krause, F., & Rädler, K.-H. 1980, Mean-Field
Magnetohydrodynamics and Dynamo Theory (Oxford:
Pergamon Press)

Moffatt, H. K. 1978, Magnetic Field Generation in
Electrically Conducting Fluids (Cambridge: Cambridge
University Press)

Ossendrijver, M., Stix, M., Brandenburg, A., & Rüdiger, G.
2002, A&A, 394, 735, doi: 10.1051/0004-6361:20021224

Parker, E. N. 1955, ApJ, 122, 293, doi: 10.1086/146087

—. 1979, Cosmical Magnetic Fields: Their Origin and Their
Activity (Oxford: Clarendon Press)

Pencil Code Collaboration, Brandenburg, A., Johansen, A.,
et al. 2021, JOSS, 6, 2807, doi: 10.21105/joss.02807

Pipin, V. V. 2023, MNRAS, 522, 2919,
doi: 10.1093/mnras/stad1150

Pouquet, A., Frisch, U., & Leorat, J. 1976, JFM, 77, 321,
doi: 10.1017/S0022112076002140

Rädler, K. H. 1969, Monatsber. Deutsch. Akad Wissensch.
Berlin, 11, 194

Rheinhardt, M., & Brandenburg, A. 2010, A&A, 520, A28,
doi: 10.1051/0004-6361/201014700

—. 2012, Astron. Nachr., 333, 71,
doi: 10.1002/asna.201111625

Rincon, F. 2021, PhRvF, 6, L121701,
doi: 10.1103/PhysRevFluids.6.L121701

Rogachevskii, I., & Kleeorin, N. 2003, PhRvE, 68, 036301,
doi: 10.1103/PhysRevE.68.036301

—. 2004, PhRvE, 70, 046310,
doi: 10.1103/PhysRevE.70.046310

Rüdiger, G., & Brandenburg, A. 2014, PhRvE, 89, 033009,
doi: 10.1103/PhysRevE.89.033009

Rüdiger, G., & Kichatinov, L. L. 1993, A&A, 269, 581

Schrinner, M., Rädler, K. H., Schmitt, D., Rheinhardt, M.,
& Christensen, U. 2005, Astron. Nachr., 326, 245,
doi: 10.1002/asna.200410384

Schrinner, M., Rädler, K.-H., Schmitt, D., Rheinhardt, M.,
& Christensen, U. R. 2007, GApFD, 101, 81,
doi: 10.1080/03091920701345707

Shukurov, A., & Subramanian, K. 2022, Astrophysical
Magnetic Fields: From Galaxies to the Early Universe
(Cambridge: Cambridge University Press)

Squire, J., & Bhattacharjee, A. 2015, PhRvE, 92, 053101,
doi: 10.1103/PhysRevE.92.053101

Steenbeck, M., Krause, F., & Rädler, K. H. 1966, Zeitschr.
Naturforsch. A, 21, 369, doi: 10.1515/zna-1966-0401

Stefani, F., & Gerbeth, G. 2003, PhRvE, 67, 027302,
doi: 10.1103/PhysRevE.67.027302

Stepinski, T. F., & Levy, E. H. 1990, ApJ, 362, 318,
doi: 10.1086/169268

Vishniac, E. T., & Cho, J. 2001, ApJ, 550, 752,
doi: 10.1086/319817

Warnecke, J., Rheinhardt, M., Viviani, M., et al. 2021,
ApJL, 919, L13, doi: 10.3847/2041-8213/ac1db5

Zeldovich, Ya. B., Ruzmaikin, A. A., & Sokoloff, D. D.
1983, Magnetic Fields in Astrophysics (New York:
Gordon and Breach)

Zenati, Y., & Vishniac, E. T. 2023, ApJ, 948, 11,
  doi: 10.3847/1538-4357/acca1e

Zhou, H., & Blackman, E. G. 2024, PhRvE, 109, 015206,
  doi: 10.1103/PhysRevE.109.015206